Synthesis, Structure and Properties of the High-pressure Modifications of the Ternary Compounds *RE*PtSn (*RE* = La, Pr, Sm)

Jan F. Riecken[a], Ute Ch. Rodewald[a], Gunter Heymann[b], Sudhindra Rayaprol[a], Hubert Huppertz[b], Rolf-Dieter Hoffmann[a], and Rainer Pöttgen[a]

[a] Institut für Anorganische und Analytische Chemie, Universität Münster, Corrensstraße 30, D-48149 Münster, Germany
[b] Department Chemie und Biochemie, Ludwig-Maximilians-Universität München, Butenandtstraße 5 – 13 (Haus D), 81377 München, Germany

Reprint requests to Prof. Dr. R. Pöttgen. E-mail: pottgen@uni-muenster.de

Z. Naturforsch. **61b,** 1477 – 1484 (2006); received August 21, 2006

The hexagonal high-pressure (HP) modifications of the ternary compounds *RE*PtSn (*RE* = La, Pr, Sm) were prepared under multianvil high-pressure (9 – 14 GPa) high-temperature (1050 – 1400 °C) conditions from the orthorhombic normal-pressure (NP) modifications. The HP-*RE*PtSn stannides were investigated by X-ray diffraction on powders and single crystals: ZrNiAl type, space group $P\bar{6}2m$, $a = 762.6(2)$, $c = 418.55(7)$ pm, $wR2 = 0.1147$, 256 F^2 values and 14 variables for HP-LaPtSn, $a = 754.97(7)$, $c = 412.64(3)$ pm, $wR2 = 0.0782$, 252 F^2 values and 14 variables for HP-PrPtSn, and $a = 750.1(2)$, $c = 407.6(1)$ pm, $wR2 = 0.1060$, 229 F^2 values and 14 variables for HP-SmPtSn. The high-pressure modifications have two crystallographically independent platinum positions in trigonal prismatic coordination, $Pt1Sn_6RE_3$ and $Pt2Sn_3RE_6$. The shortest interatomic distances occur between the platinum and tin atoms within the three-dimensional [PtSn] networks. The rare earth atoms fill distorted hexagonal channels within these networks and they are bound through short *RE*-Pt contacts. Susceptibility measurements of HP-PrPtSn reveal paramagnetic behaviour with an experimental magnetic moment of 3.31(2) μ_B/Pr atom. Low-temperature susceptibility and specific heat data point to inhomogeneous magnetism in HP-PrPtSn.

Key words: Intermetallic Compounds, Magnetism, High-pressure Phases

Introduction

The equiatomic *RE*PtSn (*RE* = rare earth element) stannides have first been synthesized by Dwight and coworkers some thirty years ago [1] and preliminary magnetic studies were performed in the Yakinthos group [2]. Later, these stannides have intensively been studied with respect to their interesting magnetic and electronic properties. A good literature overview is given in [3 – 6, and ref. therein].

With La, Ce, Pr, Nd, Sm, or Eu as rare earth metal components, these stannides crystallize with the orthorhombic TiNiSi-type structure [7], while those with the smaller rare earth elements adopt the hexagonal ZrNiAl-type [8 – 10]. This change in crystal structure seems to be driven by the size of the rare earth elements (lanthanoid contraction). For CePtSn [5] and NdPtSn [6] we could recently show that the phase transition can also occur through application of high-pressure and high-temperature. Since this is a reconstructive phase transition, the high-pressure samples can easily be quenched and characterized under ambient pressure conditions.

We have now extended our investigations with respect to the *RE*PtSn stannides with *RE* = La, Pr, Sm, in order to complete the series. So far, only X-ray powder data of LaPtSn [11, 12] and PrPtSn [2, 13] have been reported, while no lattice parameters can be found in the literature for SmPtSn [14]. Herein we report on crystallographic and physical property studies of the normal- and high-pressure phases *RE*PtSn (*RE* = La, Pr, Sm).

Experimental Section

Synthesis

Starting materials for the synthesis of the normal-pressure modifications of LaPtSn, PrPtSn, and SmPtSn were ingots of the rare earth metals (Chempur or Johnson Matthey), platinum powder (Degussa-Hüls, 200 mesh), and a tin bar (Her-

Table 1. Crystal data and structure refinement for NP-*RE*PtSn (*RE* = La, Pr, Sm), space group *Pnma*, $Z = 4$.

Empirical formula	NP-LaPtSn	NP-PrPtSn	NP-SmPtSn
Molar mass [g/mol]	452.69	454.69	464.13
Unit cell dimensions [pm]	$a = 755.8(1)$	$a = 742.81(6)$	$a = 731.6(2)$
(powder data)	$b = 465.7(1)$	$b = 461.77(4)$	$b = 459.1(2)$
	$c = 805.3(1)$	$c = 802.30(5)$	$c = 801.1(3)$
V [nm^3]	0.2835	0.2752	0.2691
Calculated density [g/cm^3]	10.61	10.97	11.46
Crystal size [μm^3]	$20 \times 30 \times 60$	$20 \times 30 \times 30$	$20 \times 20 \times 30$
Detector distance [mm]	60	60	–
Exposure time [min]	5	6	–
ω Range; increment [°]	0 – 180; 1.0	0 – 180; 1.0	–
Transm. ratio (max/min)	0.490 / 0.138	0.335 / 0.193	0.923 / 0.178
Absorption coefficient [mm^{-1}]	72.4	76.8	82.2
$F(000)$	740	748	760
θ Range [°]	3 to 35	3 to 35	3 to 35
Range in *hkl*	$-12/+11$, $-7/+6$, ±12	±11, ±7, $-12/+11$	±11, $-7/0$; ±12
Total no. reflections	3869	3870	2413
Independent reflections	683 ($R_{int} = 0.0367$)	653 (R_{int}0.0594)	641 ($R_{int} = 0.1021$)
Reflections with $I \geq 2\sigma(I)$	552 ($R_{sigma} = 0.0405$)	511 ($R_{sigma} = 0.0480$)	611 ($R_{sigma} = 0.0653$)
Data/parameters	683 / 20	653 / 20	641 / 20
Goodness-of-fit on F^2	0.897	0.867	1.046
Final R indices [$I \geq 2\sigma(I)$]	$R1 = 0.0252$	$R1 = 0.0286$	$R1 = 0.0234$
	$wR2 = 0.0541$	$wR2 = 0.0470$	$wR2 = 0.0453$
R indices (all data)	$R1 = 0.0368$	$R1 = 0.0457$	$R1 = 0.0251$
	$wR2 = 0.0558$	$wR2 = 0.0500$	$wR2 = 0.0459$
Extinction coefficient	0.0067(3)	0.0026(2)	0.0034(2)
Largest diff. peak and hole [e/Å^3]	$2.76/-3.86$	$3.24/-3.44$	$3.48/-3.30$

Table 2. Crystal data and structure refinement for HP-*RE*PtSn (*RE* = La, Pr, Sm), space group *P*62*m*, $Z = 3$.

Empirical formula	HP-LaPtSn	HP-PrPtSn	HP-SmPtSn
Molar mass [g/mol]	452.69	454.69	464.13
Unit cell dimensions [pm]	$a = 762.6(2)$	$a = 754.97(7)$	$a = 750.1(2)$
(powder data)	$c = 418.55(7)$	$c = 412.64(3)$	$c = 407.6(1)$
V [nm^3]	0.2108	0.2037	0.1986
Calculated density [g/cm^3]	10.70	11.12	11.64
Crystal size [μm^3]	$20 \times 20 \times 40$	$20 \times 20 \times 60$	$20 \times 20 \times 20$
Transm. ratio (max/min)	0.705 / 0.453	0.315 / 0.297	0.252 / 0.069
Absorption coefficient [mm^{-1}]	73.0	77.8	83.5
$F(000)$	555	561	570
θ Range [°]	3 to 30	3 to 30	3 to 29
Range in *hkl*	±10, ±10, ±5	±10, ±10, ±5	±10, ±10, ±5
Total no. reflections	2279	3233	2140
Independent reflections	256 ($R_{int} = 0.1939$)	252 ($R_{int} = 0.2026$)	229 ($R_{int} = 0.3491$)
Reflections with $I \geq 2\sigma(I)$	221 ($R_{sigma} = 0.0757$)	225 ($R_{sigma} = 0.0600$)	204 ($R_{sigma} = 0.1421$)
Data/parameters	256/14	252/14	229/14
Goodness-of-fit on F^2	1.218	1.171	1.031
Final R indices [$I \geq 2\sigma(I)$]	$R1 = 0.0495$	$R1 = 0.0345$	$R1 = 0.0457$
	$wR2 = 0.0978$	$wR2 = 0.0708$	$wR2 = 0.0985$
R indices (all data)	$R1 = 0.0693$	$R1 = 0.0471$	$R1 = 0.0583$
	$wR2 = 0.1147$	$wR2 = 0.0782$	$wR2 = 0.1060$
Flack parameter x	$-0.04(5)$	$-0.04(1)$	$-0.01(5)$
Extinction coefficient	0.0001(7)	0.0012(4)	0.002(1)
Largest diff. peak and hole [e/Å^3]	$4.27/-4.86$	$3.09/-3.02$	$4.89/-6.80$

aeus), all with stated purities better than 99.9%. The larger rare earth metal ingots were mechanically cut into smaller pieces under paraffin oil and cleaned with *n*-hexane. Both the paraffin oil and *n*-hexane were dried over sodium wire. The small rare earth metal pieces were subsequently arc-melted under an atmosphere of *ca.* 600 mbar argon [15]. The argon was purified over molecular sieves, silica gel, and titanium sponge (900 K). The pre-melting procedure for the rare earth metals strongly reduces a shattering of these elements during the exothermic reaction with platinum and tin. The rare earth metal buttons, cold-pressed pellets of platinum (∅6 mm) and pieces of the tin bar were then mixed in

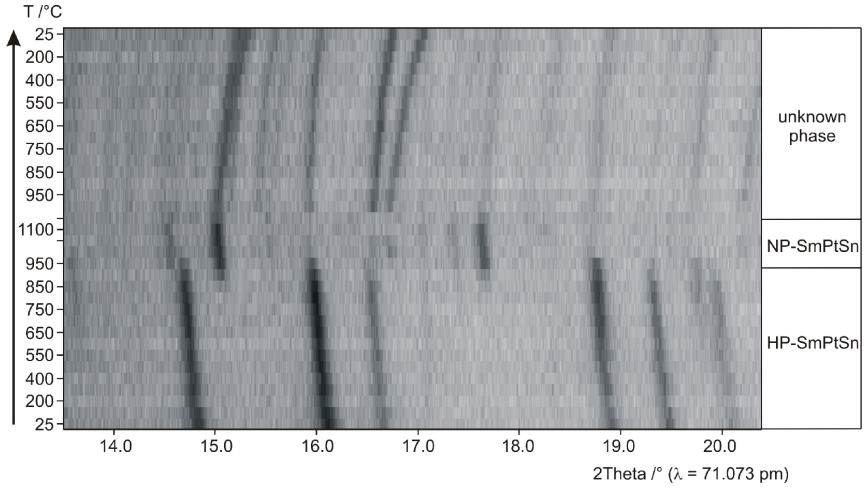

Fig. 1. Temperature-dependent X-ray powder patterns of HP-SmPtSn.

the ideal 1 : 1 : 1 atomic ratio and the stannides were synthesized by arc-melting of the elements. The samples were then flipped over and remelted in order to achieve homogeneity. The moisture stable samples were obtained in amounts of 1 g.

The high-pressure/high-temperature treatment of the phases NP-*RE*PtSn (*RE* = La, Pr, Sm) took place *via* a multianvil assembly. Details about the technique and the construction of the different assemblies can be found in references [16 – 19]. In order to realize the phase transformations, the intermetallic normal-pressure precursors were carefully milled and filled into boron nitride crucibles of the high-pressure assemblies. The intermetallic samples were compressed to pressures of 11.5 GPa (HP-LaPtSn; 14/8-assembly), 10.5 GPa (HP-PrPtSn; 14/8-assembly), and 13.5 GPa (HP-SmPtSn; 10/5-assembly) for 240 min. In principle, all mentioned phases can be synthesized in the pressure range 9 – 14 GPa. In contrast to HP-PrPtSn and HP-SmPtSn, which were obtained as phase-pure compounds, the lanthanum compound up to now appeared always as a mixture of the normal- and high-pressure form (with HP-LaPtSn being the major phase). The synthesis temperatures varied in the range of 1050 – 1400 °C (HP-LaPtSn: 1050 °C; HP-PrPtSn: 1100 °C; HP-SmPtSn: 1400 °C). Within 20 min the maximum temperature was reached followed by a 10 min period of constant temperature. Afterwards, the samples were cooled to r. t. within 10 min. Systematic investigations showed that higher temperatures and subsequent annealing under pressure at 500 to 900 °C for several hours enhanced the crystallinity of the samples. After decompression, the samples were carefully separated under a microscope from the surrounding assembly parts.

NP-*RE*PtSn and HP-*RE*PtSn (*RE* = La, Pr, Sm) are stable in moist air over weeks. The polycrystalline samples are silvery with metallic luster. Powdered samples of both modifications are dark gray.

X-Ray diffraction

The samples were characterized through Guinier powder patterns using CuK_{α_1} radiation and α-quartz ($a = 491.30$, $c = 540.46$ pm) as an internal standard. The orthorhombic, respectively hexagonal lattice parameters (Tables 1 and 2) were obtained from least-squares fits of the powder data. The correct indexing of the patterns was ensured through intensity calculations [20] taking the atomic positions from the structure refinements. The lattice parameters determined from the powders and the single crystals agreed well and were also in good agreement with the literature data.

Temperature dependent *in situ* X-ray diffractometry was performed for the HP-SmPtSn sample on a STOE Stadi P powder diffractometer (MoK_α; $\lambda = 71.073$ pm) with a computer-controlled STOE furnace. An electrically heated graphite tube held the sample capillary vertical with respect to the scattering plane. Bores in the graphite tube permitted unobstructed pathways for the primary beam as well as for the scattered radiation. The temperature, measured by a thermocouple in the graphite tube, was kept constant within 0.2 °C. The heating rate between different temperatures was set to 50 °C/min and the data acquisition started directly after reaching the next temperature step.

Successive heating of HP-SmPtSn filled in a 0.1 mm outside diameter Mark capillary showed that the high-pressure modification was stable up to 850 °C under argon atmosphere (Fig. 1). The complete transformation into the normal-pressure modification took place at about 1000 °C. Interestingly, HP-SmPtSn transformed back to the normal-pressure modification at temperatures about 150 °C higher than isotypic HP-CePtSn [5]. In contrast to HP-CePtSn, where the transformation into the normal-pressure phase started at 500 °C and ended up at 850 °C, the samarium compound retransformed in a smaller range between 850 – 1000 °C. At

Table 3. Atomic coordinates and anisotropic displacement parameters (pm^2) for NP-*RE*PtSn (*RE* = La, Pr, Sm). U_{eq} is defined as one third of the trace of the orthogonalized U_{ij} tensor. The anisotropic displacement factor exponent takes the form: $-2\pi^2[(ha^*)^2U_{11}+\ldots+2hka^*b^*U_{12}]$. $U_{12}=U_{23}=0$.

Atom	Wyckoff position	*x*	*y*	*z*	U_{11}	U_{22}	U_{33}	U_{13}	U_{eq}
NP-LaPtSn									
La	4*c*	0.01293(8)	1/4	0.69532(7)	49(3)	59(2)	48(2)	3(2)	52(1)
Pt	4*c*	0.29273(6)	1/4	0.40883(5)	73(2)	44(2)	46(2)	−1(1)	54(1)
Sn	4*c*	0.17590(9)	1/4	0.08304(9)	63(3)	36(3)	36(3)	−2(2)	45(1)
NP-PrPtSn									
Pr	4*c*	0.01117(9)	1/4	0.69785(8)	94(3)	96(2)	117(3)	3(2)	102(1)
Pt	4*c*	0.28722(6)	1/4	0.40766(6)	109(2)	80(2)	85(2)	1(2)	91(1)
Sn	4*c*	0.17551(10)	1/4	0.08176(11)	122(3)	80(3)	85(4)	4(3)	96(2)
NP-SmPtSn									
Sm	4*c*	0.01070(4)	1/4	0.69735(6)	71(1)	75(1)	33(2)	2(1)	60(1)
Pt	4*c*	0.28729(3)	1/4	0.40942(4)	90(1)	60(1)	27(2)	−2(1)	59(1)
Sn	4*c*	0.17866(6)	1/4	0.08367(7)	88(2)	52(2)	12(3)	−2(2)	51(1)

Table 4. Atomic coordinates and anisotropic displacement parameters (pm^2) for HP-*RE*PtSn (*RE* = La, Pr, Sm). U_{eq} is defined as one third of the trace of the orthogonalized U_{ij} tensor. The anisotropic displacement factor exponent takes the form: $-2\pi^2[(ha^*)^2U_{11}+\ldots+2hka^*b^*U_{12}]$. $U_{13}=U_{23}=0$.

Atom	Wyckoff position	*x*	*y*	*z*	U_{11}	U_{22}	U_{33}	U_{12}	U_{eq}
HP-LaPtSn									
La	3*f*	0.5859(5)	0	0	24(11)	45(16)	37(13)	23(8)	33(7)
Pt1	1*a*	0	0	0	36(10)	U_{11}	51(16)	18(5)	41(7)
Pt2	2*d*	2/3	1/3	1/2	49(7)	U_{11}	58(12)	24(4)	52(6)
Sn	3*g*	0.2490(5)	0	1/2	22(12)	13(17)	37(17)	7(8)	25(7)
HP-PrPtSn									
Pr	3*f*	0.4110(3)	0	0	44(7)	56(10)	68(10)	28(5)	55(5)
Pt1	1*a*	0	0	0	46(6)	U_{11}	54(12)	23(3)	49(5)
Pt2	2*d*	1/3	2/3	1/2	46(5)	U_{11}	101(10)	23(2)	64(4)
Sn	3*g*	0.7473(3)	0	1/2	35(8)	31(11)	63(14)	16(6)	44(5)
HP-SmPtSn									
Sm	3*f*	0.5919(4)	0	0	114(11)	136(13)	29(13)	68(6)	91(7)
Pt1	1*a*	0	0	0	107(9)	U_{11}	5(17)	53(5)	73(7)
Pt2	2*d*	2/3	1/3	1/2	104(7)	U_{11}	62(14)	52(4)	90(6)
Sn	3*g*	0.2558(4)	0	1/2	72(11)	119(16)	29(19)	60(8)	68(8)

the maximum temperature of 1100 °C, another transformation into an unknown phase took place. Under these conditions a reaction with the Mark capillary could not be excluded. No further transformations of the unknown phase were detectable by lowering the temperature to ambient conditions.

Single crystal intensity data were collected at r. t. by use of a four-circle diffractometer (CAD4) with graphite monochromatized MoK_α (71.073 pm) radiation and a scintillation counter with pulse height discrimination. The scans were taken in the $\omega/2\theta$ mode and empirical absorption corrections were applied on the basis of psi-scan data, followed by spherical absorption corrections. Some crystals were measured on a Stoe IPDS-II image plate system in oscillation mode. Numerical absorption corrections were applied to these data sets. All relevant details concerning the data collections and evaluations are listed in Tables 1 and 2.

Structure refinements

Small, irregularly shaped single crystals of the normal- and high-pressure modifications of *RE*PtSn (*RE* = La, Pr, Sm) were first examined by use of a Buerger camera equipped with an image plate system (Fujifilm BAS-1800) in order to establish both symmetry and suitability for intensity data collection. For HP-SmPtSn it was extremely difficult to find a suitable single crystal. Most investigated crystals consisted of several domains. The isotypy of the normal-pressure modifications with the orthorhombic TiNiSi-type [7], space group *Pnma*, and of the high-pressure modifications with the hexagonal ZrNiAl-type [8 – 10], space group $P\bar{6}2m$, was already evident from the Guinier powder data.

The atomic parameters of isotypic NP-CePtSn and HP-CePtSn [5] were taken as starting values and the structures were refined using SHELXL-97 [21] (full-matrix least-squares on F^2) with anisotropic atomic displacement parameters for all atoms. Refinement of the correct absolute structure for the high-pressure modifications was ensured through refinement of the Flack *x* parameter [22, 23]. As a check for the correct composition and the correct site assignment, the occupancy parameters were refined in separate series of least-squares cycles along with the displacement parameters. All sites were fully occupied within two standard deviations and in the final cycles the ideal occupancies were assumed again. The final difference Fourier syntheses were flat (Tables 1 and 2). The positional parameters and interatomic distances (exemplary for LaPtSn) of the refinements are listed in Tables 3 – 5. Further details on the structure refinements are available.

Table 5. Interatomic distances (pm), calculated with the powder lattice parameters in NP- and HP-LaPtSn. Standard deviations are given in parentheses. All distances within the first coordination spheres are listed.

NP-LaPtSn				HP-LaPtSn			
La:	1	Pt	313.0(1)	La:	4	Pt2	310.7(1)
	2	Pt	324.6(1)		1	Pt1	315.8(4)
	2	Sn	326.3(1)		2	Sn	331.4(4)
	1	Sn	335.7(1)		4	Sn	345.9(3)
	2	Pt	338.6(1)		4	La	397.8(2)
	1	Sn	339.3(1)		2	La	418.6(1)
	2	Sn	343.1(1)				
	1	Pt	359.6(1)				
	2	La	388.0(1)				
	2	La	391.9(1)				
Pt:	2	Sn	272.9(1)	Pt1:	6	Sn	282.6(2)
	1	Sn	276.8(1)		3	La	315.8(4)
	1	Sn	289.7(1)	Pt2:	3	Sn	291.8(2)
	1	La	313.0(1)		6	La	310.7(1)
	2	La	324.6(1)				
	2	La	338.6(1)				
	1	La	359.6(1)				
Sn:	2	Pt	272.9(1)	Sn:	2	Pt1	282.6(2)
	1	Pt	276.8(1)		2	Pt2	291.8(2)
	1	Pt	289.7(1)		2	Sn	328.8(6)
	2	La	326.3(1)		2	La	331.4(4)
	1	La	335.7(1)		4	La	345.9(3)
	1	La	339.3(1)				
	2	La	343.1(1)				

Details may be obtained from: Fachinformationszentrum Karlsruhe, D-76344 Eggenstein-Leopoldshafen (Germany), by quoting the Registry No's. CSD-416896 (NP-LaPtSn), CSD-416901 (HP-LaPtSn), CSD-416898 (NP-PrPtSn), CSD-416900 (HP-PrPtSn), CSD-416897 (NP-SmPtSn), and CSD-416899 (HP-SmPtSn).

Physical property measurements

The physical properties of HP-PrPtSn were studied by magnetic susceptibility and heat capacity (C_p) measurements on a Quantum Design Physical Property Measurement System (PPMS). The sample for magnetic measurements was enclosed in a gelatin capsule and attached to the sample rod of the AC measurement system (ACMS). For the C_p measurement the sample was glued to the platform of a precalibrated heat capacity measuring puck using *Apiezon N* grease.

Results and Discussion

Crystal chemistry

Similar to HP-CePtSn [5] and HP-NdPtSn [6], the orthorhombic stannides LaPtSn, PrPtSn, and SmPtSn also transform to ZrNiAl-type high-pressure modifications. As is evident from Fig. 2, the transformation is accompanied by a densification effect of less that 1% in volume. The course of the cell volumes of the normal-pressure and high-pressure phases nicely reflects the lanthanoid contraction. Both curves are almost parallel. As expected for the trivalent cerium atoms on both CePtSn modifications, the plot of the cell volumes shows no anomaly. The samarium compound has now been fully characterized for the first time. In their previous study, Sakurai *et al.* [14] did not report lattice parameters.

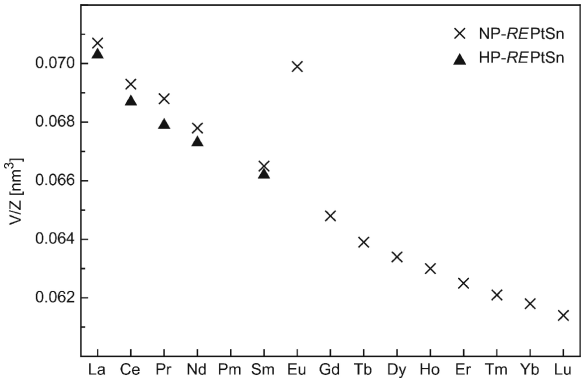

Fig. 2. Plot of the cell volumes of the orthorhombic normal- and hexagonal high-pressure modifications of *RE*PtSn. For better comparison we plot the volumes per formula unit.

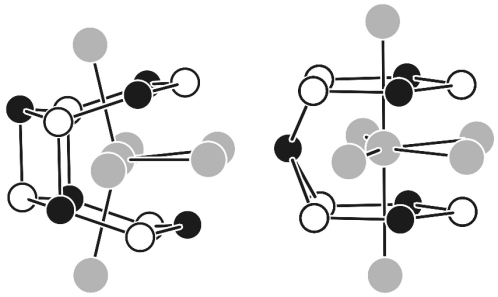

Fig. 3. Coordination polyhedra of the lanthanum atoms in NP-LaPtSn and HP-LaPtSn. The site symmetries are indicated.

The crystal chemistry details and a discussion of chemical bonding in both modifications had already been given for CePtSn [5]. Here we give only a brief account. As an example, the lanthanum coordination polyhedra of both modifications are presented in Fig. 3. Due to the reconstructive type of the phase transition we observe a significantly different coordination. Each lanthanum atom has six nearest lanthanum neighbors,

but in different geometry and with distinctly different La–La distances (Table 5). Also the lanthanum–platinum coordination is different, *i. e.* six platinum neighbors in the normal-pressure and five in the high-pressure modification. The different rare earth coordination is the main reason for the differing magnetic properties of both modifications of PrPtSn, similar to CePtSn [5] and NdPtSn [6].

Magnetic properties of HP-PrPtSn

The magnetic behavior of NP-PrPtSn was studied on polycrystalline samples [2] and a Czochralski grown single crystal [13]. The detailed studies by Janušova *et al.* [13] gave no hint for magnetic ordering down to 0.4 K.

In Fig. 4, we present the dc (χ) of HP-PrPtSn measured in an applied dc field of 5 kOe. The susceptibility $\chi(T)$ increases monotonously with decreasing temperature, as expected for a paramagnet. Below 10 K a broad step-like anomaly appears, however, without any clear signature of magnetic ordering. From the linear region of the inverse susceptibility at temperatures above 100 K, the paramagnetic Curie temperature observed is about -4.5 K. The negative sign indicates an-

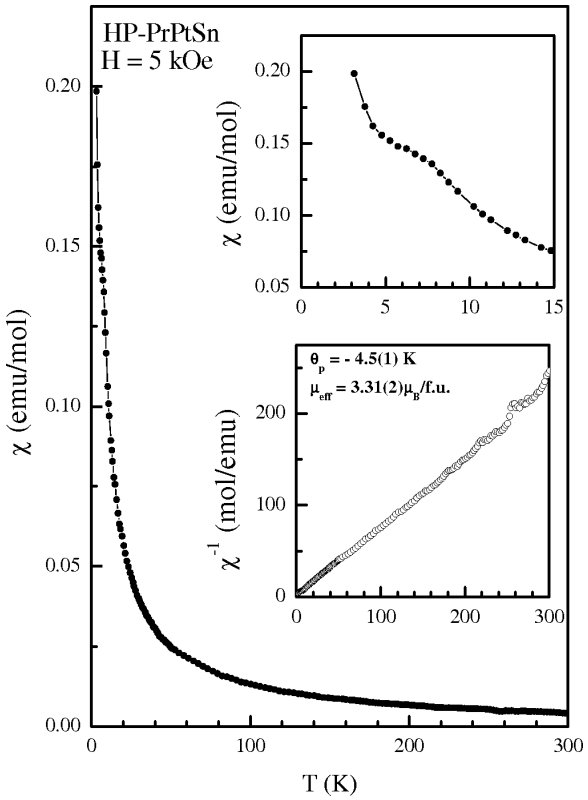

Fig. 4. The dc susceptibility ($\chi = M/H$) as a function of temperature (T) for HP-PrPtSn measured in a steady field of 5 kOe. The top inset shows the anomaly in $\chi(T)$ at low temperatures. The bottom inset shows the inverse susceptibility in the measured temperature range.

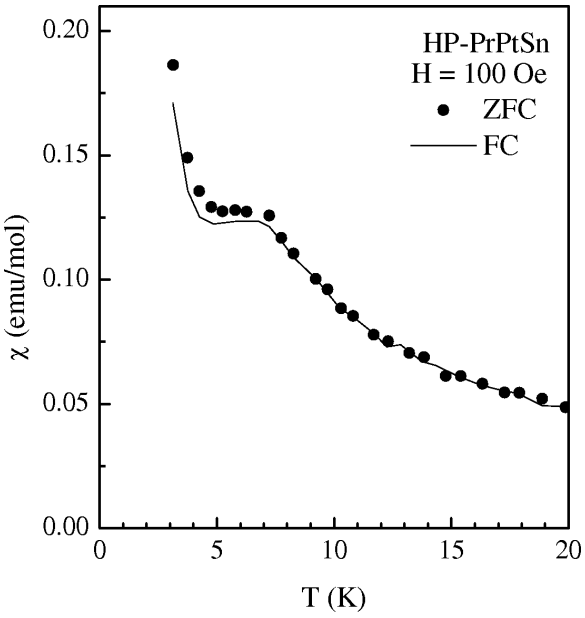

Fig. 5. The dc susceptibility ($\chi = M/H$) of HP-PrPtSn measured in ZFC-FC state of the sample at a dc field of 100 Oe.

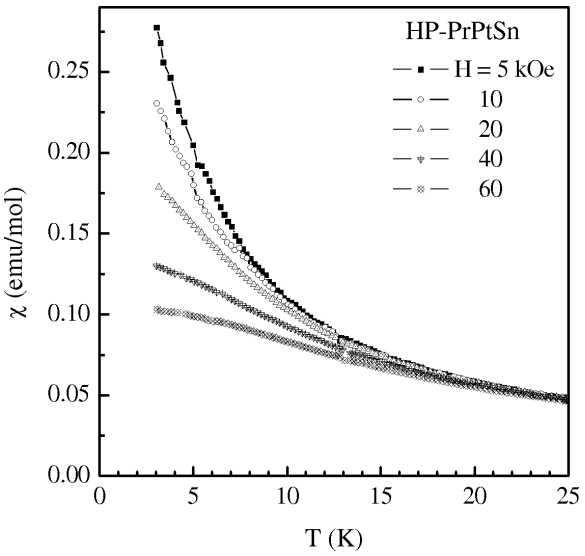

Fig. 6. The dc susceptibility ($\chi = M/H$) of HP-PrPtSn measured in ZFC state of the sample at several applied fields.

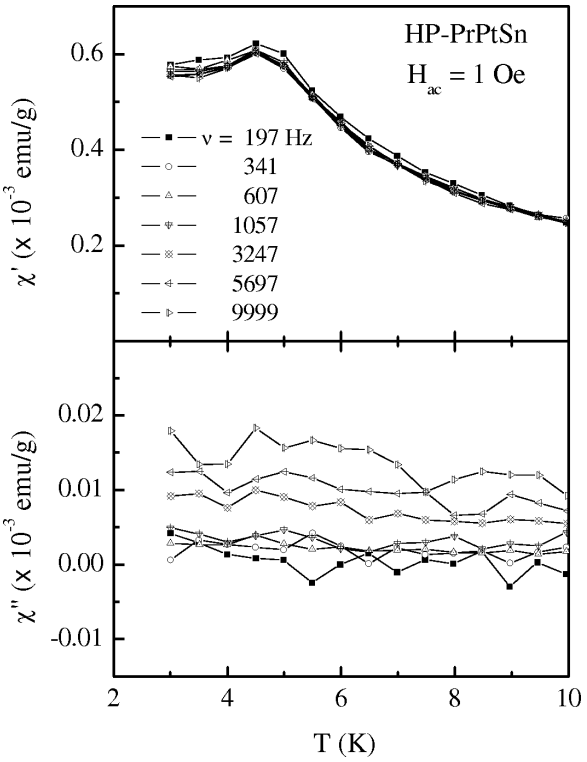

Fig. 7. The ac susceptibility of HP-PrPtSn measured in an ac field (H_{ac}) of 1 Oe and at different driving frequencies (ν).

tiferromagnetic interactions. The effective Bohr magneton number (μ_B) per Pr^{3+} calculated from the inverse susceptibility is 3.31(2) μ_B close to the theoretical value of 3.58 μ_B. In contrast, the investigations on NP-PrPtSn data [2, 13] revealed an experimental magnetic moment slightly higher than the theoretical one.

The anomaly below 10 K is more clearly visible in the $\chi(T)$ curve measured at a low field of 100 Oe (Fig. 5). The $\chi(T)$ data measured in ZFC and FC states of the sample do not bifurcate and are the same within the experimental errors. The peak in the diagram of the 100 Oe measurements appears near 10 K, as compared to the 5 kOe measurement. To probe response of this anomaly to the dc field, we have measured $\chi(T)$ of HP-PrPtSn at different applied fields and plotted these data in Fig. 6. The figure clearly shows the field dependence of the susceptibility. The moment values (in emu/mol) decrease with increasing field. The step in $\chi(T)$ observed for $H \leq 10$ kOe also vanished with increasing field. The overlap of the ZFC-FC curves $\chi(T)$ in low field rules out any spin-glass anomalies. Therefore, the origin of the broad feature below 10 K can

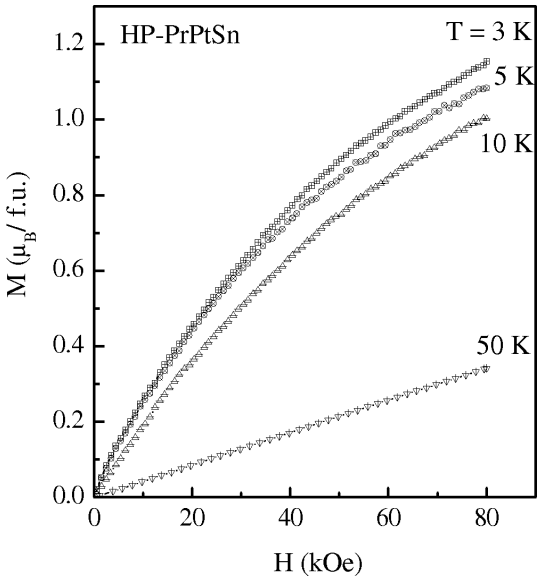

Fig. 8. Magnetization (M) as a function of varying field (H) for HP-PrPtSn, measured at various temperatures.

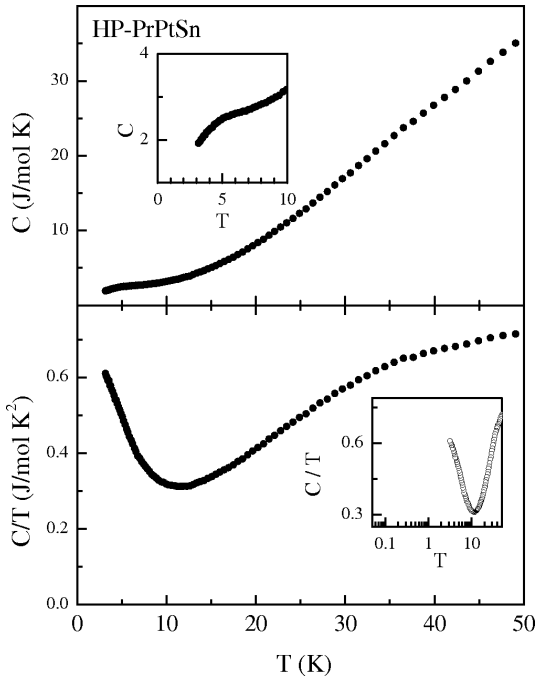

Fig. 9. Specific heat (C_p) of HP-PrPtSn plotted as C_p *vs.* T and C_p/T *vs.* T in the top and bottom panels. The inset in the top panel highlights the features below 10 K. The inset in the bottom panel is shown to highlight the logarithmic increase in C_p/T at low temperatures (below 10 K).

be due to short range magnetic ordering arising due to inhomogeneous magnetism.

We present here the ac susceptibility (χ' and χ'') data of HP-PrPtSn measured at different frequencies and an ac field (amplitude, H_{ac}) of 1 Oe. In Fig. 7, we have plotted the real and imaginary parts of the linear susceptibility (χ' and χ''). The broad peak around 6 K is consistent with the step-like feature in the dc susceptibility. The two main observations from this measurement are (i) no frequency dependence in χ' and (ii) featureless χ''. This rules out quite conclusively any type of spin-glass like anomaly in HP-PrPtSn.

We have also measured isothermal magnetizations of HP-PrPtSn at several temperatures. In Fig. 8, we show the $M(H)$ data measured after reaching the temperature in ZFC state. For $T \leq 10$ K, isotherms increase non-linearly with increasing H, the sample thus behaving as an antiferromagnet without saturation up to 80 kOe. The moment value at 80 kOe and 3 K is about 1.1 μ_B, about 30% of the expected saturation moment for Pr^{3+} (given by $g \times J = 3.20\ \mu_B$). The features of $M(H)$ are similar up to $T = 10$ K, which indicates the persistence of inhomogeneous magnetism up to 10 K. At 50 K, $M(H)$ is linear indicative of a paramagnetic state.

Now we focus on the $C_p(T)$ of HP-PrPtSn in Fig. 9. The anomalies observed in the magnetic measurements can also be seen for C_p in the form of a broad peak around 5 K. We also show the plot of C_p/T *vs.* T in the same figure. The absence of any clear peak is indicative of inhomogeneous magnetism in HP-PrPtSn. Stewart *et al.* [24] have shown that one of the signatures for non-Fermi liquid behavior in an intermetallic compound with $d-f$ electrons is a $-\log T$ temperature-dependence of C_p (*i. e.*, an upturn in the plot of C_p/T *vs.* $\log T$). In the inset of the bottom panel, we illustrate the C_p/T *vs.* T correlation, with T plotted on a log scale to highlight $C_p/T \sim -\log T$ at low temperatures. Thus, the C_P data are in line with the susceptibility data.

Acknowledgements

We thank Prof. W. Schnick for using the high-pressure facilities, Dipl.-Chem. B. V. Lotsch and T. Miller for the *in situ* X-ray diffractometry, S. Christian for preparative help, and H.-J. Göcke for the work at the scanning electron microscope. This work was financially supported by the Deutsche Forschungsgemeinschaft (Po573/10-1 and HU966/4-1) and the European Science Foundation through the COST D30/003/03 network *Development of Materials Chemistry using High-Pressures*. S. Rayaprol is indebted to the Alexander von Humboldt-Stiftung for a research grant.

[1] A. E. Dwight, W. C. Harper, C. W. Kimball, J. Less-Common Met. **30**, 1 (1973).
[2] Ch. D. Routsi, J. K. Yakinthos, E. Gamari-Seale, J. Magn. Magn. Mater. **110**, 317 (1992).
[3] A. Szytuła, J. Leciejewicz, Handbook of Crystal Structures and Magnetic Properties of Rare Earth Intermetallics. CRC Press, Boca Raton, Florida (1994).
[4] R. V. Skolozdra, Stannides of rare-earth and transition metals, in K. A. Gschneidner (Jr.), L. Eyring (eds): Handbook on the Physics and Chemistry of Rare Earths, North-Holland/Elsevier, Amsterdam, Vol. 24, chapter 164, 399 – 517 (1997).
[5] J. F. Riecken, G. Heymann, T. Soltner, R.-D. Hoffmann, H. Huppertz, D. Johrendt, R. Pöttgen, Z. Naturforsch. **60b**, 821 (2005).
[6] G. Heymann, S. Rayaprol, J. F. Riecken, R.-D. Hoffmann, U. Ch. Rodewald, H. Huppertz, R. Pöttgen, Solid State Sci., in press.
[7] C. B. Shoemaker, D. P. Shoemaker, Acta Crystallogr. **18**, 900 (1965).
[8] P. I. Krypyakevich, V. Ya. Markiv, E. V. Melnyk, Dopov. Akad. Nauk. Ukr. RSR, Ser. A 750 (1967).
[9] A. E. Dwight, M. H. Mueller, R. A. Conner (Jr.), J. W. Downey, H. Knott, Trans. Met. Soc. AIME **242**, 2075 (1968).
[10] M. F. Zumdick, R.-D. Hoffmann, R. Pöttgen, Z. Naturforsch. **54b**, 45 (1999).
[11] F. Canepa, S. Cirafici, J. Alloys Compd. **232**, 71 (1996).
[12] M. Divis, B. Janoušova, J. Rusz, V. Sechovsky, M. Richter, I. Opahle, J. Alloys Compd. **376**, 28 (2004).
[13] B. Janoušova, V. Sechovsky, A. H. Lacerda, T. Komatsubara, Czech. J. Phys. **54 (Suppl. D)**, D319 (2004).
[14] J. Sakurai, K. Kegai, T. Kuwai, Y. Isikawa, K. Nishimura, K. Mori, J. Magn. Magn. Mater. **140 – 144**, 875 (1995).
[15] R. Pöttgen, Th. Gulden, A. Simon, GIT Labor-Fachzeitschrift **43**, 133 (1999).
[16] H. Huppertz, Z. Kristallogr. **219**, 330 (2004).
[17] D. Walker, M. A. Carpenter, C. M. Hitch, Am. Mineral. **75**, 1020 (1990).
[18] D. Walker, Am. Mineral. **76**, 1092 (1991).
[19] D. C. Rubie, Phase Trans. **68**, 431 (1999).
[20] K. Yvon, W. Jeitschko, E. Parthé, J. Appl. Crystallogr. **10**, 73 (1977).
[21] G. M. Sheldrick, SHELXL-97, Program for Crystal Structure Refinement, University of Göttingen, 1997.
[22] H. D. Flack, G. Bernadinelli, Acta Crystallogr. **A55**, 908 (1999).
[23] H. D. Flack, G. Bernadinelli, J. Appl. Crystallogr. **33**, 1143 (2000).
[24] G. R. Stewart, Rev. Mod. Phys. **73**, 797 (2001).